Ab initio analysis of autoionization of H_3 molecules using multichannel quantum-defect theory and new quantum-defect surfaces

I. Mistrík, R. Reichle, U. Müller,* and H. Helm
Fakultät für Physik, Albert-Ludwig-Universität Freiburg, Stefan-Meier-Strasse 19, 79104 Freiburg, Germany

M. Jungen†
Institute of Physical Chemistry, University of Basel, Klingelbergstrasse 80, CH-4056 Basel, Switzerland

J. A. Stephens‡
Nuclear Data Section, Department of Nuclear Sciences and Applications, International Atomic Energy Agency, P.O. Box 100, Wagramer Strasse 5, A-1400 Vienna, Austria

(Received 6 August 1999; published 15 February 2000)

Highly accurate Born-Oppenheimer potential-energy surfaces of H_3 were calculated and combined with multichannel quantum-defect theory (MQDT) to predict with high precision the photoionization cross section of laser-excited triatomic hydrogen recently measured in this laboratory. The experiment first prepares H_3 in stepwise excitation in a single rotational level of the symmetric stretch excited 3*s* Rydberg state. One-photon ionization from this state populates the continuum and *np* Rydberg states which autoionize into $H_3^+ + e^-$. In the vicinity of the first symmetric stretch excited level of H_3^+ the ionization spectrum shows features similar to those observed at the lowest ionization threshold: a quasidiscrete region below the first symmetric-stretch excited threshold, a Beutler-Fano region of rotational autoionization and interlopers of low-*n* Rydberg states belonging to high vibrationally excited cores dispersed over the continuum. The MQDT calculations include rotational, vibrational, and Jahn-Teller interactions, and permit the assignment of most of the spectral features.

PACS number(s): 33.80.Rv, 33.80.Eh

I. INTRODUCTION

The optical spectrum of the H_3 molecule was discovered by Herzberg in a hollow cathode discharge [1]. Numerous low-lying Rydberg states were found and assigned in emission in gas discharges as well as in fast-beam studies [2–4]. The higher Rydberg states and ionization potentials of H_3 were investigated using photoionization spectroscopy [4–6]. A specific interest in understanding the spectrum of neutral H_3 above the ionization threshold arises from its relevance to the dissociative recombination (DR) process, $H_3^+ + e^- \rightarrow H + H_2$ and $H + H + H$. Predissociation channels which energetically lie in the ionization continuum can compete with autoionization of highly excited H_3. These two processes follow the inverse paths of electron capture and inelastic electron-core collisions which control DR. At least a selected range of Rydberg states are believed to be strongly coupled to the repulsive ground state of H_3 and directly involved in DR [7–10]. The yet unsolved dependence of dissociative recombination on electron energy and on vibrational excitation [11] makes it particularly interesting to analyze Rydberg spectra converging to rovibrationally excited H_3^+ cores.

The dynamics of Rydberg levels with low electronic angular momentum is dominated by short-range e^--ion interactions, while for Rydberg states with higher electronic angular momentum only the long-range interactions are effective. Polarization models employing perturbation theory [12] can generally be used to describe the dynamics of high angular momentum electrons. However for low-*l* states such as the *np*-Rydberg series discussed here, theoretical methods which incorporate short-range e^--ion interactions are required. This is the reason why we have employed the multichannel quantum-defect theory (MQDT) approach here.

MQDT has been extensively applied to treat the Rydberg spectra of atoms [13], and a comprehensive review of this theory has recently been given by Aymar *et al.* [14]. Fano initially adapted MQDT to the H_2 molecule [15]. Jungen discussed the MQDT formalism for the H_2 molecule starting from the full molecular Hamiltonian [16], and accounted for the rovibronic level structure of several low-lying H_2 Rydberg states. Numerous calculations have been performed to treat autoionization phenomena in H_2 [17–19]. It is also possible to incorporate predissociation channels and dissociative recombination processes [20–25] within the MQDT approach. Fano and Lu initially sketched the application of QDT to triatomic hydrogen [26], and two-channel QDT for rotational *l* uncoupling in triatomic hydrogen was discussed by Lu and Pan [27] and by Reichle *et al.* [28]. By incorporating full extensions needed to treat rotational *l* uncoupling, two-channel QDT was applied to a first analysis of the *p*-Rydberg series of H_3 by Bordas *et al.* [29]. Their experimental ionization spectrum of H_3 $3s\ A_1'$ $(N'=1,K'=0,\{0,0^0\}) \rightarrow H_3^+ + e^-$ showed the strong influence of rotational and vibrational autoionization. [Here the notation $(N,K,\{\nu_1,\nu_2^{l_2}\})$ is adapted to describe the rovibrational ex-

*Electronic address: Ulrich.Mueller@physik.uni-freiburg.de
†Electronic address: Martin.Jungen@unibas.ch
‡Electronic address: j.a.stephens@iaea.org

citation in the symmetric stretch mode ν_1, the asymmetric stretch mode ν_2, and the vibrational angular momentum l_2. N is the total angular momentum of the molecule, and K is the projection of N to the molecular top axis.] Stephens and Greene [30,31] formulated a MQDT frame transformation for H_3 molecules which includes full rotational, vibrational, and Jahn-Teller interactions. They showed that inclusion of the latter interaction is required to account for a portion of the resonances observed by Bordas *et al.* [29]. The quantum-defect functions used in these studies were derived from the extensive set of Born-Oppenheimer potential energy surfaces calculated by Nager and Jungen [32].

Recently we have measured photoionization spectra for the process

$$H_3\ \ 3s\ \ A_1'\ \ (N'=1,K'=0,\{1,0^0\})+h\nu_2\rightarrow {H_3}^+ + e^- \tag{1.1}$$

at energies between 340 and 500 meV above the lowest ionization threshold, and used two-channel QDT including rotational interactions for its preliminary analysis [28]. The purpose of the present paper is to report a full MQDT analysis of this spectrum based on new, highly accurate *ab initio* Born-Oppenheimer potential surfaces for the lowest np Rydberg states of the H_3 molecule. The results of these *ab initio* calculations are also presented in this paper. Combining these new *ab initio* data for the $np\ \ A_2''$ and npE' potential surfaces of H_3 with accurate rovibrational energies of the ionic core [33,34], and the MQDT developed for the H_3 molecule [31], a satisfactory representation of the experimental photoionization spectrum is obtained.

By comparing the experimental and calculated spectra we demonstrate the applicability of MQDT methods to treat Rydberg spectra of small polyatomic molecules. MQDT proves to be an extremely useful tool to assign and understand the nature of resonances and perturbations appearing in the Rydberg spectra.

II. EXPERIMENT

Details of the experiment have been discussed previously [28] so only a brief discussion pertinent to the present paper is given here. A fast beam of metastable triatomic hydrogen molecules is merged coaxially over a length of 130 cm with two pulsed-laser beams. A first photon excites the long-lived vibrationless metastable level $2p\ \ A_2''$ $(N''=0,K''=0,\{0,0^0\})$ to the $3s\ \ A_1'$ $(N'=1,K'=0,\{1,0^0\})$ state in an off-diagonal vibrational transition. A second photon excites this selected $3s$ level to the ionization continuum. A detector monitors ${H_3}^+$ ions which are formed along the interaction region as a result of autoionization or direct photoionization. This detector records the total ionization spectrum and does not discriminate the different rovibrational final-state channels of ${H_3}^+$. However, some control of the total angular momentum of the final state is achieved through the choice of the relative orientation of the polarization of the two lasers (see below).

III. *Ab-initio* POTENTIAL-ENERGY AND QUANTUM-DEFECT SURFACES

To perform MQDT calculations including the vibrational and Jahn-Teller interactions needed for the interpretation of the spectra, quantum-defect surfaces as functions of nuclear geometry and of electronic energy for the np excited states of H_3 covering an appropriate part of the space of the internal coordinates were calculated. The quantum defect μ of a Rydberg state is defined as the deviation of its effective quantum number (as obtained from the ionization energy using the inverse of a generalized Balmer formula) from the corresponding theoretical integer: $n_{eff}=n-\mu$. Quantum defects comprise information about the phase shift of Rydberg and continuum electronic wave functions with respect to the hydrogenic case. As a rule quantum defects are only slightly energy dependent and can frequently be considered constant to a good approximation. In order to obtain precise quantum defects, high-quality energy differences between the excited states and the ${H_3}^+$ ion are needed. In Basel a new series of computations which produced highly correlated electronic wave functions using the multireference CEPA program of Fink and Staemmler [35] was carried out. The basis consisted of a Dunning cc-pVQZ standard set for each atom [36], augmented by Kaufmann Rydberg functions [37] centered at the center of positive charge of the parent ion ${H_3}^+$ with all angular momenta up to g functions and principal quantum numbers up to $n=6$. The total basis consisted of 290 (in part) contracted Gaussian functions; 200 of them are used to represent the various Rydberg orbitals of H_3. The electronic energies have been computed at the CEPA-0 level, using multiconfiguration reference wave functions. Although the CEPA program is able to evaluate expectation values of single-particle operators with correlated wave functions, the computation of properties of the wave function such as electronic transition moments and the angular momentum analysis for the Rydberg orbitals have been restricted to the self-consistent-field level.

Based on past experience with similar calculations [31] a subset of the grid points used by Dykstra and Swope [38] was chosen for the representation of the surfaces. This subset is documented in Table I; we show both the normal coordinates defined in Ref. [38] and—in order to allow an easier understanding—the corresponding bond length coordinates. Note that we have used a different numbering scheme for the grid points than Dykstra and Swope. The set comprises a cut along the totally symmetric S normal coordinate including the equilibrium geometry of the ${H_3}^+$ ion, a series of obtuse and acute C_{2v} triangles, and a number of C_s arrangements.

The angular-momentum composition of the various Rydberg orbitals was analyzed using the method described by Kaufmann and Baumeister [39]. It turned out that nearly all Rydberg orbitals relevant for this study are l-pure np or $3s$ functions to better than 90%, most of them even better than 98%. This is an important condition for the use of a united atom nomenclature for the orbitals of H_3. Though not a requirement, this condition results in an important simplification of MQDT calculations (see Ref. [31]). Only for a few extreme grid points is there considerable orbital mixing such

TABLE I. Grid points used for the representation of potential-energy surfaces.

Symm.	No. [a]	Dykstra coordinates [a]			Bond-length coordinates (units of a_o)		
Eq. [b]	1	0.0000	0.0	0	1.6504	1.6504	1.6504
D_{3h}	2	-0.2964	0.0	0	1.137	1.137	1.137
	3	-0.2158	0.0	0	1.277	1.277	1.277
	4	-0.1367	0.0	0	1.414	1.414	1.414
	5	-0.0584	0.0	0	1.549	1.549	1.549
	6	-0.0037	0.0	0	1.644	1.644	1.644
	7	0.0002	0.0	0	1.651	1.651	1.651
	8	0.0032	0.0	0	1.656	1.656	1.656
	9	0.0975	0.0	0	1.819	1.819	1.819
	10	0.2559	0.0	0	2.094	2.094	2.094
	11 [c]	0.3374	0.0	0	2.235	2.235	2.235
C_{2v}	12 [c]	0.0	0.3000	0	2.170	1.462	1.462
	13	0.0	0.2000	0	1.997	1.507	1.507
	14	0.0	0.1500	0	1.910	1.537	1.537
	15	0.0	0.1000	0	1.824	1.571	1.571
	16	0.0	0.0500	0	1.737	1.609	1.609
	17	0.0	0.0500	60	1.695	1.695	1.564
	18	0.0	0.1000	60	1.743	1.743	1.477
	19	0.0	0.1500	60	1.794	1.794	1.391
	20	0.0	0.2000	60	1.848	1.848	1.304
	21 [c]	0.0	0.3000	60	1.962	1.962	1.131
C_s	22	0.0	0.0546	30	1.733	1.653	1.569
	23	0.0	0.0546	45	1.719	1.677	1.559
	24	0.0	0.1091	45	1.789	1.709	1.469
	25	0.0	0.1637	12	1.929	1.586	1.476
	26	0.0	0.1637	48	1.852	1.759	1.374
	27	0.0	0.2182	24	2.002	1.654	1.363
	28 [c]	0.0	0.3273	50	2.061	1.920	1.907

[a] S/a_o, R/a_o, $\theta/°$ (see Refs. [38,32]); our numbering of the grid points is different from these authors.

[b] Experimental equilibrium geometry of H_3^+ [1,52,53].

[c] Grid points with a strong mixing of Rydberg orbitals with different angular momenta (see text). Neighboring points are also mixed to a lesser extent (see Table III).

TABLE II. CEPA energies (a.u.) for the H_3^+ ion and for the $2p$ components of H_3.

No.	H_3^+	$2p_x$ [a]	$2p_y$ [b]	$2p_z$ [c]
1	−1.34315	−1.56194		−1.47778
2	−1.23264	−1.40567		−1.36825
3	−1.29452	−1.47988		−1.43009
4	−1.32663	−1.52383		−1.46198
5	−1.34054	−1.55001		−1.47553
6	−1.34313	−1.56133		−1.47780
7	−1.34315	−1.56197		−1.47778
8	−1.34214	−1.56245		−1.47776
9	−1.33776	−1.57221		−1.47164
10	−1.31409	−1.57355		−1.44647
11	−1.29821	−1.57014		−1.42970
12	−1.31715	−1.60450	−1.48589	−1.45036
13	−1.32963	−1.59462	−1.51125	−1.46356
14	−1.33498	−1.58841	−1.52428	−1.46921
15	−1.33927	−1.58101	−1.53727	−1.47371
16	−1.34211	−1.57219	−1.54989	−1.47670
17	−1.34197	−1.54928	−1.57255	−1.47655
18	−1.33816	−1.53467	−1.58166	−1.47258
19	−1.33117	−1.51750	−1.58853	−1.46533
20	−1.32035	−1.49724	−1.59236	−1.45414
21	−1.28333	−1.44412	−1.58647	−1.41610
22	−1.34183	−1.54844	−1.57266	−1.47640
23	−1.34177	−1.54829	−1.57336	−1.47634
24	−1.33735	−1.53244	−1.58297	−1.47173
25	−1.33315	−1.51999	−1.59007	−1.46727
26	−1.32912	−1.51340	−1.58993	−1.46318
27	−1.32342	−1.50067	−1.59537	−1.45717
28	−1.27208	−1.42953	−1.58284	−1.40454

[a] e' in D_{3h}, b_2 in C_{2v}, and a' in C_s symmetry.

[b] e' in D_{3h}, a_1 in C_{2v}, and a' in C_s symmetry.

[c] a_2'' in D_{3h}, b_1 in C_{2v}, and a'' in C_s symmetry.

that united atom $3s$ and np orbitals can no longer be identified unambiguously. Such points are marked in the tables.

Total energies for the parent ion and the three components of $2p$ are given in Table II. For the equilibrium geometry our total energy of H_3^+ is about 150 cm^{-1} higher than the very accurate results of Cencek *et al.* [33]. Table III shows the effective quantum numbers of np states of H_3 for higher principal quantum numbers n up to 5. At equilibrium the electronic states not documented here are arranged as follows: The ns states are just below the corresponding npa'', the nd, nf, and ng have nearly integer effective quantum numbers and are located between the $(n-1)pa''$ and the npe'. This ordering holds for nearly all geometries considered. Electron correlation (not accounted for in our earlier calculations [32]) shifts the quantum defects of the np states quite uniformly by about 0.05 units. Note that the np_z quantum defects (perpendicular to the molecular plane) are nearly independent of energy and geometry, in contrast to the in-plane np components.

Except for a few extreme points where the Rydberg series are perturbed the effective quantum numbers exhibit a satisfying regularity. Their near-integer steps not only demonstrate the high quality of the results but also indicate a slight (geometry-dependent) energy dependence of the quantum defects. However, variation of an effective quantum number of about 5 by 0.01 units corresponds to an energy shift of less than 20 cm^{-1}, which is clearly below the precision of the calculations (the calculated quantum numbers are obtained as differences of two independent quantum-chemical calculations). A linear extrapolation of the quantum defects using $3p$ and $4p$ values seems to be possible if quantum defects outside the energy range covered by our calculations are needed. In this way we obtain for the quantum defect functions at equilibrium geometry: $\mu_{pa''}(\epsilon)=0.06-0.09\epsilon, \mu_{pe'}(\epsilon)=0.38-0.32\epsilon$ where ϵ is the energy in a.u. with respect to the ionization limit.

Petsalakis *et al.* [40] carried out MRD-CI calculations for

TABLE III. Effective quantum numbers for the $3p$, $4p$, and $5p$ Rydberg states of H_3. From these numbers both the quantum defects and the total energies (using the energy of H_3^+) can be constructed.

No.	$3p_x$	$3p_y$	$3p_z$	$4p_x$	$4p_y$	$4p_z$	$5p_x$	$5p_y$	$5p_z$
1	2.593		2.932	3.605		3.934	4.609		4.936
2	2.713		2.920	3.717		3.919	4.717		4.921
3	2.676		2.921	3.681		3.921	4.683		4.923
4	2.642		2.924	3.650		3.925	4.653		4.927
5	2.613		2.928	3.623		3.930	4.627		4.932
6	2.595		2.932	3.606		3.933	4.610		4.936
7	2.593		2.932	3.605		3.933	4.609		4.936
8	2.592		2.932	3.604		3.933	4.607		4.937
9	2.564		2.939	3.576		3.941	4.579		4.943
10	2.567		2.953	3.587		3.942	4.595		4.945
11 [a]	2.555		2.961	3.577		3.964	4.585		4.968
12 [b]	2.489	2.743	2.941	3.512	3.745	3.941	4.520	4.749	4.945
13	2.517	2.701	2.936	3.536	3.705	3.937	4.543	4.707	4.940
14	2.533	2.662	2.934	3.551	3.684	3.935	4.557	4.686	4.938
15	2.551	2.639	2.933	3.567	3.647	3.934	4.572	4.647	4.937
16	2.571	2.616	2.932	3.585	3.625	3.933	4.590	4.627	4.936
17	2.618	2.570	2.932	3.627	3.584	3.933	4.629	4.588	4.936
18	2.644	2.547	2.933	3.651	3.563	3.934	4.653	4.568	4.937
19	2.673	2.524	2.935	3.677	3.542	3.935	4.676	4.548	4.939
20	2.703	2.502	2.938	3.705	3.521	3.937	4.705	4.528	4.942
21 [c]	2.765	2.459	2.935	3.763	3.500	3.947	4.763	4.509	4.949
22	2.619	2.569	2.932	3.628	3.582	3.933	4.629	4.587	4.936
23	2.620	2.568	2.932	3.629	3.582	3.933	4.631	4.586	4.936
24	2.649	2.543	2.933	3.655	3.559	3.934	4.657	4.565	4.937
25	2.669	2.527	2.935	3.691	3.546	3.935	4.693	4.552	4.939
26	2.680	2.519	2.935	3.683	3.537	3.936	4.682	4.544	4.940
27	2.700	2.505	2.938	3.720	3.525	3.937	4.722	4.532	4.942
28 [c]	2.779	2.466	2.951	3.776	3.491	3.949	4.775	4.501	4.951

[a] $4,5pa_2''$ exchanged with $4,5fa_2''$. Diabatic values: $4pa_2''$ and $5pa_2''$.

[b] The npa_1 series has only about 80% p character.

[c] The np_z series is strongly mixed with d functions.

the surfaces of a number of Rydberg states of H_3. Unfortunately comparison is difficult, as the parent ion (the natural reference energy for Rydberg states) is not documented in this paper. Our total energies seem to be lower by about 0.007 a.u., and the errors of the energy differences between the Rydberg states quoted by these authors are considerably improved in the present work.

IV. MQDT THEORY

In this section we summarize the main theoretical elements relevant to our MQDT analysis. The applicability of the MQDT approach hinges on separation of the e^--ion interaction into two spatial regions, depending on a radial distance r compared to r_0, i.e., the reaction surface at which the Rydberg electron interaction with the ionic core becomes purely Coulombic [15–18]. Outside the reaction zone ($r > r_0$) the interaction between the Rydberg electron and the ionic electrons can be neglected. Within the reaction zone ($r < r_0$) the Rydberg electron is indistinguishable from the ionic electrons, and electronic motion is approximately separable from nuclear motion. In this region the electronic wave functions, potential-energy, and quantum-defect surfaces as functions of nuclear geometry, can be calculated using the Born-Oppenheimer (BO) approximation and *ab initio* quantum-chemical methods, as discussed in Sec. III. In the reaction zone the Rydberg electron can exchange energy or angular momentum with the core electrons and nuclei, but as it emerges beyond r_0, its wave function is phase shifted compared to a pure Coulomb wave, due to *all* core interactions. The matching of a linear combination of the short-range, BO ''eigenchannels'' Ψ_α to linear combinations of states representing the scattering (decay) channels Ψ_i for $r \sim r_0$ yields the required phase information (reaction matrices $K_{i,i'}$) needed to describe inelastic processes such as rotational and vibrational autoionization. For most molecular MQDT calculations to date, implicit in this matching procedure is the assumption of a reaction matrix which varies smoothly with total energy E, and is usually taken to be energy independent. Furthermore, with that assumption, the boundary r_0 need not be specified explicitly, but typically it is of order $r_0 \sim 5a_0$. Physically the energy independence re-

sults from the local kinetic energy of the Rydberg electron in the reaction zone greatly exceeding the differences in core rovibrational energies. Under these circumstances, the frame transformation elements $U_{i\alpha}$ can be obtained semianalytically, and the spectral mixing coefficients $A_{\alpha\rho}$ can be efficiently computed by solution of a generalized eigenvalue problem [18].

Computationally then the MQDT approach to electron-ion collisions obtains a laboratory-frame reaction matrix $K_{i,i'}$ for scattering from one fragmentation channel i into alternative channels i'. The i'th independent solution $\Psi_{i'}(E)$ of the Schrödinger equation is written for $r>r_0$ as

$$\Psi_{i'}(E)=\mathcal{A}r^{-1}\sum_{i=1}^{N_t}\Phi_i(\omega)[f_i(r)\delta_{ii'}-g_i(r)K_{i,i'}], \tag{4.1}$$

where the coordinate r is the radial distance between the excited electron and the H_3^+ center of mass, and the function $\Phi_i(\omega)$ specifies a rovibronic state of the H_3^+ core and angular part of the Rydberg electron wave function coupled with the rotational wave function of the ion. $\mathcal{A}$ is the antisymmetrization operator, and ω represents all other spin and spatial coordinates for the ionic core and the angular and spin coordinates of the excited electron. The functions $f_i(r)$ and $g_i(r)$ are the energy normalized regular and irregular Coulomb wave functions, respectively. The reaction matrix $K_{i,i'}$ is typically a smooth function of the total energy E, and, as discussed above, it is taken to be independent of the Rydberg electron energy.

We determine the reaction matrix $K_{i,i'}$ by a rovibrational frame transformation with elements

$$U_{i,\alpha}=\langle i|\alpha\rangle=\langle v^+\Gamma^+|\mathbf{Q}\rangle^{(N^+K^+)}\langle N^+K^+|\Lambda\rangle^{(N_fl_f)}, \tag{4.2}$$

where $\langle v^+\Gamma^+|\mathbf{Q}\rangle^{(N^+K^+)}$ is the complex conjugate of an ionic vibrational wave function (written in a space representation), $\langle N^+K^+|\Lambda\rangle^{(N_fl_f)}=U^{(N_fl_f)}_{N^+K^+,\Lambda}$ is the rotational component of the frame transformation, and integration over coordinates $\mathbf{Q}$ is implied when summing over the index α. $\mathbf{Q}$ specifies the nuclear vibrational coordinates [see Eq. (5.2)]. The full frame transformation for the reaction matrix is then [31]

$$\langle v^+\Gamma^+N^+K^+|\mathbf{K}|v^{+\prime}\Gamma^{+\prime}N^{+\prime}K^{+\prime}\rangle^{(N_fl_f)} \tag{4.3}$$

$$=\sum_{\Lambda,\Lambda'}U^{(N_fl_f)}_{N^+K^+,\Lambda}\langle v^+\Gamma^+|K_{\Lambda,\Lambda'}|v^{+\prime}\Gamma^{+\prime}\rangle(\tilde{\mathbf{U}})^{(N_fl_f)}_{\Lambda',N^{+\prime}K^{+\prime}}, \tag{4.4}$$

where the vibrational matrix elements are

$$\langle v^+\Gamma^+|K_{\Lambda,\Lambda'}|v^{+\prime}\Gamma^{+\prime}\rangle = \int d\mathbf{Q}\chi^*_{v^+\Gamma^+}(\mathbf{Q})K_{\Lambda,\Lambda'}(\mathbf{Q})\chi_{v^{+\prime}\Gamma^{+\prime}}(\mathbf{Q}). \tag{4.5}$$

and $\chi_{v^{+\prime}\Gamma^{+\prime}}(\mathbf{Q})$ is the ionic vibrational wave function. The rotational frame transformation elements from Hund's case (b) to case (d) coupling are given by

$$(\tilde{\mathbf{U}})^{(N_fl_f)}_{\Lambda,N^+K^+}=\left[\frac{2N_f+1}{(1+\delta_{\Lambda0}\delta_{K^+0})}\right]^{-1/2}\left[\frac{2N^++1}{(1+\delta_{K^+0})}\right]^{1/2} \times\langle l_f\Lambda,N^+K^+|N_f\Lambda+K^+\rangle, \tag{4.6}$$

where the last factor in Eq. (4.6) is a Clebsh-Gordan coefficient. In Eqs. (4.4)–(4.6) l_f is the orbital angular momentum of the excited (Rydberg or continuum) electron, Λ is the projection of this angular momentum on a chosen body-frame z axis (here the C_3 axis), and N_f is the total angular momentum of the electron-ion core system. $K_{\Lambda,\Lambda'}$ in Eq. (4.5) is a nuclear-geometry-dependent reaction matrix. For a p electron this matrix can be written as [31]

$$K_{\Lambda,\Lambda'}(\mathbf{Q})=\begin{pmatrix}\tan[\pi\mu_{\Lambda=0}(\mathbf{Q})] & 0 & 0\\ 0 & \delta\rho^2 & \lambda\rho\exp(i\phi)\\ 0 & \lambda\rho\exp(-i\phi) & \delta\rho^2\end{pmatrix}, \tag{4.7}$$

where this matrix has off-diagonal elements for $\Lambda=\pm1$. These off-diagonal elements represent the interaction between the components of the (initially) degenerate electronic state and the bending E' vibrations. The equilibrium quantum defect for p_{xy} orbitals (not shown in the above equation) is included by using a phase-renormalized base pair of Coulomb functions as discussed in Ref. [31]. In Eq. (4.7) λ and δ are the linear Jahn-Teller splitting constant and frequency shift parameter, respectively, and ρ and ϕ are radial and azimuthal normal coordinates defined in Eq. (5.2). The above treatment accounts for vibrational interactions within nondegenerate Rydberg series and for Jahn-Teller interactions between doubly degenerate Rydberg series. Inclusion of the Jahn-Teller interaction also allows indirect excitation of Rydberg series converging to the nontotally symmetric vibrationally excited states of H_3^+.

The dipole transition amplitude from an initial state specified by quantum numbers $\{v_i\Gamma_iN_iK_i\rho_i\}$ to a eigenchannel state $|\alpha\rangle$ with final-state angular momentum N_f is

$$d_{\alpha}^{(N_f)} = \sum_{v^+\Gamma^+N^+K^+} (\tilde{\mathbf{U}})_{\alpha,\Gamma^+v^+N^+K^+}^{(N_f)} \times \sum_{\Lambda} \langle N^+K^+|\Lambda\rangle^{(N_f l_f)} d_{\Lambda\rho_f\rho_i}^{(N_f)}, \tag{4.8}$$

where $(\tilde{\mathbf{U}})_{\alpha,\Gamma^+v^+N^+K^+}^{(N_f)}$ is an element of the αth eigenvector of the $K_{i,i'}$ matrix, v_i is the vibrational excitation of the initial state, and ρ_i represents all other quantum numbers to describe the initial state, $\langle N^+K^+|\Lambda\rangle^{(N_f l_f)}$ is a rotational frame transformation matrix element given by Eq. (4.6). In the last equation $d_{\Lambda\rho_f\rho_i}^{(N_f)}$ is the transition amplitude evaluated as a Hund's case (d) to case (b) transition.

After the reaction matrices $K_{i,i'}$ have been calculated, we determine dipole amplitudes for transitions from an initial state of total angular momentum N_i to a final state of total angular momentum N_f at energy E. The total differential oscillator strength (given in atomic units) for producing the ionic state $v^+\Gamma^+N^+K^+$ is

$$\frac{df_{v^+\Gamma^+N^+K^+\leftarrow v_i\Gamma_iN_iK_i}}{dE} = 2\omega \sum_{N_f} \sum_{\rho=1}^{N_o} \left[\sum_{\alpha=1}^{N_t} d_{\alpha}^{(N_f)} A_{\alpha\rho} \right]^2, \tag{4.9}$$

where ω is the photon energy, $d_{\alpha}^{(N_f)}$ is given by Eq. (4.8), and $A_{\alpha\rho}$ is the ρ solution vector of the linear MQDT equations in eigenchannel form [18].

Our MQDT program calculates the spectrum either for the parallel or perpendicular orientation of the excitation laser polarization with respect to the ionization laser. The transition probability for light linearly polarized along the z axis is proportional to the line strength factor [48],

$$S(N_i \rightarrow N_f) = \sum_{m,m_f} [d_{m,M}^{N_i}(\theta)\langle N_i m, 10|N_f m_f\rangle]^2, \tag{4.10}$$

where M is the projection of N_i (total angular momentum of intermediate state) onto the space-fixed z axis in a frame of reference where the quantization axis is defined by the polarization of the first laser. The first laser prepares the rotational state $|N_iM\rangle = |10\rangle$; therefore, $M=0$. The matrix element $d_{mM}^{N_i}(\theta)$ rotates the $|N_iM\rangle$ rotational state from the frame of reference defined by the first laser to the frame defined by the second laser, where θ is the angle between the polarizations of the first and second lasers. From Eq. (4.10) we can calculate the photoionization cross section $\sigma_{N_f}(\theta)$ for arbitrary angles θ using

$$\sigma_0(\theta) = \sigma_0(0°)\cos^2(\theta), \tag{4.11a}$$

$$\sigma_1(\theta) = \sigma_1(90°)\sin^2(\theta), \tag{4.11b}$$

$$\sigma_2(\theta) = \sigma_2(0°)\left(\cos^2(\theta) + \frac{3}{4}\sin^2(\theta)\right). \tag{4.11c}$$

TABLE IV. Rovibrational energies of H_3^+ used in the MQDT calculations, taken from Ref. [33].

$v_1v_2^{l2}$	$E_{1,0}$ [a]	$E_{3,0}$	$v_1v_2^{l2}$	$E_{2,2}$	$E_{3,2}$
00^0	86.93	516.72	01^1	2614.03	2876.52
10^0	3262.99	3682.47	02^2	5286.51	5566.89
02^0	4869.93	5305.08	11^1	5653.65	5909.67
20^0	6344.72	6754.57	03^1	7122.21	7393.49
03^3	7380.78	7853.80	12^2	8141.49	8424.72
12^0	7857.48	8274.12	21^1	8589.71	8840.56
04^0	9109.19	9485.54	04^2	9329.60	9771.24
30^0	9332.61	9733.62	04^4	9934.78	10203.66

[a] $E_{N^+K^+}$, energy is given in cm^{-1}.

V. PARAMETERS FOR THE MQDT CALCULATIONS

A. Ionization channels

We use the Hund's case (d) representation to assign the overall symmetry of the np Rydberg states and the dipole moment operator [41], since the motion of a highly excited Rydberg electron is appropriately described in the laboratory frame coordinate system. The np Rydberg states are excited from the $3s\ A_1'$ ($N'=1$, $K'=0$, $\{1,0^0\}$) rovibronic level with overall symmetry A_2' in the D_{3h} symmetry group. Since the dipole moment operator transforms as A_1'', the overall symmetry of each upper level must be A_2''. The symmetry of the np Rydberg states uncorrelated with the molecular frame is A_1'' [6]; therefore, the rovibrational symmetry of the H_3^+ core must be A_2'. The ortho ($I=3/2$) rovibrational ionic states with this symmetry are $(N^+,K^+,\Gamma^+)=(1,0,A_1')$, $(3,0,A_1')$, $(2,2,E')$, $(3,2,E')$, and $(2,0,A_2')$, where Γ^+ is the symmetry of the vibrational wave function of H_3^+ and I is the total nuclear spin angular momentum. The ionization channel $(2,0,A_2')$ was not included in the MQDT calculation because the reaction matrix elements

$$\langle 2,0,A_2'|K|1,0,A_1'\rangle,\ \langle 2,0,A_2'|K|3,0,A_1'\rangle,$$

$$\langle 2,0,A_2'|K|2,2,E'\rangle,\ \langle 2,0,A_2'|K|3,2,E'\rangle$$

given by Eq. (4.3) for a p electron vanish due to symmetry, and the $\langle 2,0,A_2'|K|2,0,A_2'\rangle$ matrix element has a negligible influence on the spectrum. Moreover the rovibrational energy of the $(2,0,1A_2')$ threshold is too high (~ 7500 cm^{-1} above the lowest ionization limit) to have significant influence on the present spectrum. Each rotational ionic state is combined with ten vibrational levels. Therefore, ten ionization channels are included for $N_f=0$, 20 channels for $N_f=1$, and 40 channels for $N_f=2$. In the present MQDT calculations we used the rovibrational ionic energy levels recently computed by Jaquet and co-workers [33,34]. Most of the levels were assigned as previously discussed by Tennyson and co-workers [42–44]. The assigned ionic levels used in our calculations are given in Table IV, where we have used the (approximate) quantum numbers K^+ and l_2 to label the rovibrational levels of H_3^+.

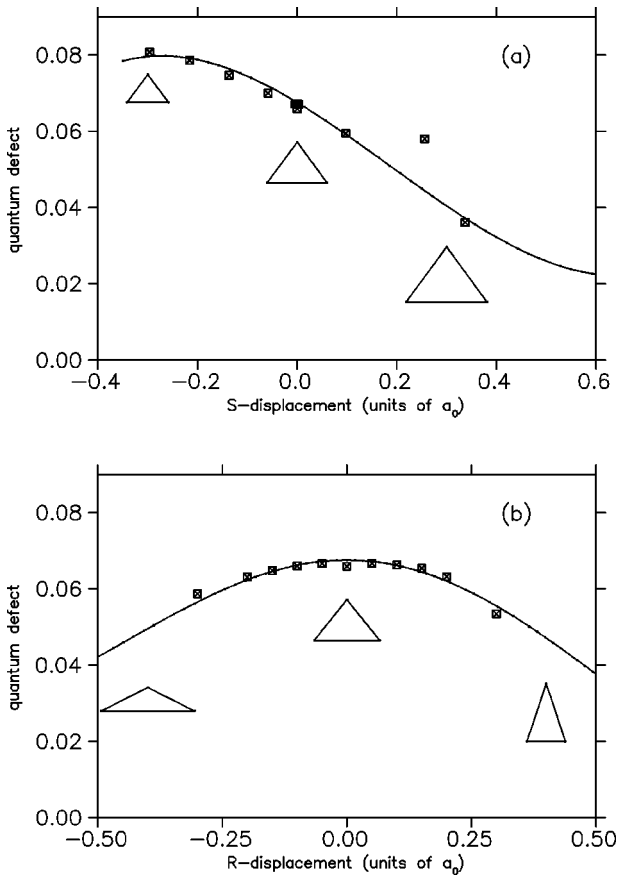

FIG. 1. *Ab initio* quantum-defect surface for the $4p\ A_2''\ (p_z)$ electronic state (symbols) along the symmetric stretch displacement coordinate S (a) and along the radial coordinate R (b) for $\theta=60°$ (positive R) and $\theta=0°$ (negative R). The solid curve is a fit using a third-order Taylor expansion. For some geometries the actual shape of internuclear coordinates is plotted for clarity.

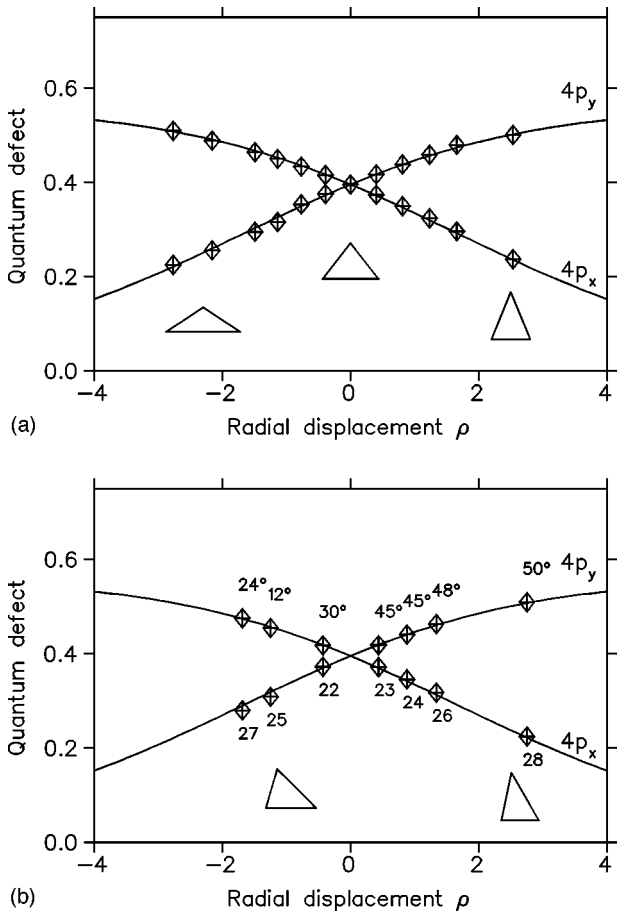

FIG. 2. *Ab initio* quantum defects of $4p_x$ and $4p_y$ orbitals (squares) showing the Jahn-Teller splitting for asymmetric stretch displacement along the A_1 mode (a) and fitted (solid line) using a two-channel MQDT model. The dimensionless radial normal coordinate ρ is defined in the text. (b) shows *ab initio* quantum defects for several nuclear configurations in C_s symmetry. These geometry points are defined in Table I. The angles ϕ and ordering numbers are also plotted for clarity.

B. Quantum-defect functions

The symmetries of np_z orbitals (perpendicular to the molecular plane) and of $np_{x,y}$ orbitals (in the molecular plane) are A_2'' and E', respectively. Furthermore, for asymmetric stretch nuclear arrangements (with symmetries E_a' and E_b') the degeneracy of the $p_{x,y}$ orbitals is lifted (Jahn-Teller effect). To evaluate the vibrational matrix elements for $\Lambda=\Lambda'=0$ in Eq. (4.5), we integrated the geometry-dependent quantum-defect surface for the $4p\ A_2''$ electronic state over the H_3^+ vibrational wave functions. The ionic vibrational wave functions were obtained using methods discussed by Spirko *et al.* [45] using the configuration-interaction potential-energy surface determined by Carney and Porter [46]. The quantum-defect surface for integration was obtained from a least squares fit of the *ab initio* quantum defects for 28 geometry points.

To describe the properties of potential functions around the equilibrium it is convenient to use orthogonal internal coordinates (S,R,θ) [38] which are related to the bond-length coordinates (r_1,r_2,r_3) through

$$r_1^2=D^2+3R^2+\sqrt{3}RD2\cos\theta, \qquad (5.1a)$$

$$r_2^2=D^2+3R^2-\sqrt{3}RD(\cos\theta-\sqrt{3}\sin\theta), \qquad (5.1b)$$

$$r_3^2=D^2+3R^2-\sqrt{3}RD(\cos\theta+\sqrt{3}\sin\theta), \qquad (5.1c)$$

where $D=\sqrt{3}(S+S_0)$ and $S_0=r_e/\sqrt{3}$. In the latter equation, r_e is the equilibrium $H-H$ distance of H_3^+, $r_e=1.6504a_0$.

The *ab initio* nuclear-geometry-dependent quantum defects were fitted in a space of stretching coordinates

TABLE V. *Ab initio* equilibrium quantum defects and Jahn-Teller splitting parameters for $np_{x,y}$ orbitals, obtained from energies in the C_{2v} geometry configuration.

State	μ_{xy}^{eq}	λ [a]	δ^a
$3p_{x,y}$	0.406	13670	1020
$4p_{x,y}$	0.395	12360	1090
$5p_{x,y}$	0.392	11950	1130

[a]Jahn-Teller splitting parameters are given in cm^{-1}.

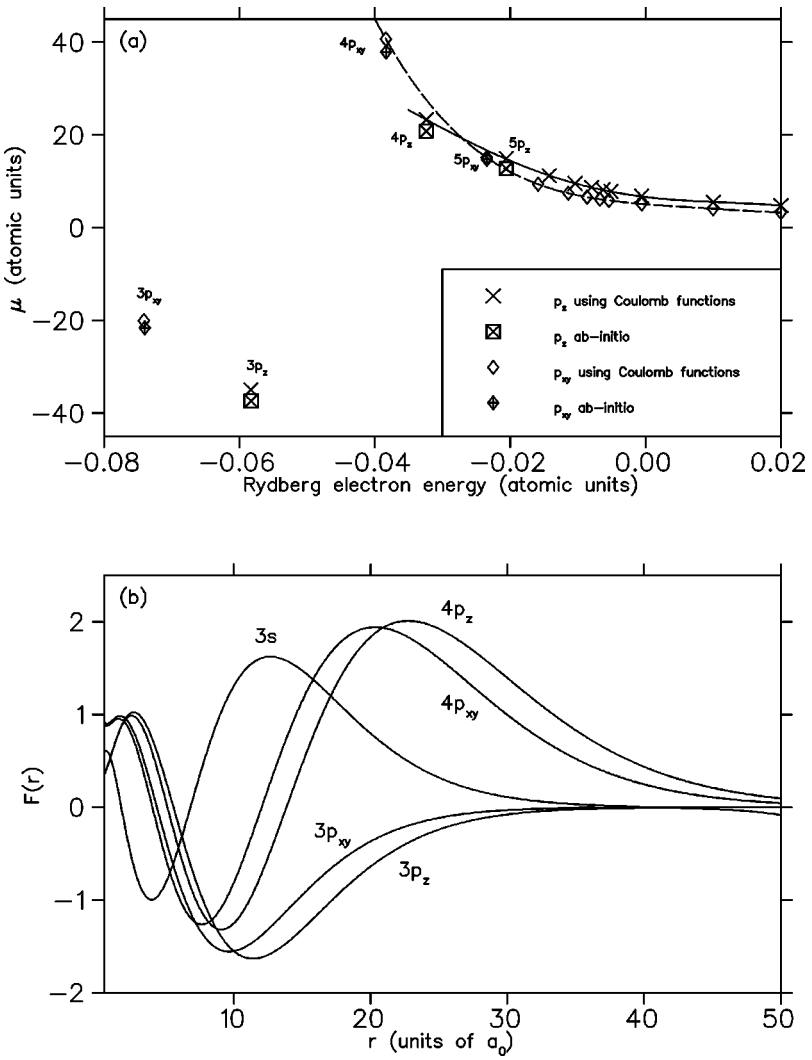

FIG. 3. Energy-normalized electronic transition dipole matrix elements $3s \rightarrow 4p_{x,y}$ at the ionic equilibrium geometry (a) calculated using phase-shifted Coulomb functions (b) as a function of the Rydberg electron energy. For $n=3-5$ we compare *ab initio* transition dipole moments with those predicted by the phase-shifted Coulomb functions.

$(\Delta r_1, \Delta r_2, \Delta r_3)$ using a third-order Taylor expansion. Here Δr_i denotes a displacement from ionic equilibrium.

The geometry points used in the fit were chosen along the symmetric stretch coordinate S, (D_{3h} geometries), along the radial coordinate R for $\theta=0°$ (obtuse triangles) and 60° (acute triangles, C_{2v} configuration) [38] and several further points covering the C_s symmetry space. The $4p_z$ quantum defect surface along the symmetric stretch (S) coordinate and along the radial (R) coordinate is represented in Fig. 1. With positive R we represent deformation for $\theta=60°$ and negative R for $\theta=0°$. We fitted the quantum-defect curve up to $R=\pm 0.6a_0$. Note that the linear configurations appear at $R=\pm 0.9a_0$. The fitted quantum-defect curve for the $4p_z$ orbital placed the calculated $N_f=0$ resonances to within $\sim 1-2$ cm^{-1} of their observed energies, even for the states with relatively low principal quantum number ($n=5-8$).

To calculate the electronic reaction matrix elements $K_{\Lambda,\Lambda'}$ (for $\Lambda,\Lambda'=\pm 1$) in Eq. (4.7), the linear Jahn-Teller splitting parameter λ, the frequency shift parameter δ, and the ionic equilibrium quantum defect μ_{xy}^{eq} for the $np_{x,y}$ orbitals are needed. We obtained the Jahn-Teller coupling constants from the fit of our improved *ab initio* $n=(3-5)p_{x,y}$ geometry-dependent Rydberg energy levels using a two-channel MQDT model for isolated doubly-degenerate Rydberg series [47]. We fitted the $p_{x,y}$ *ab initio* orbital energies along the radial coordinate R up to $R=\pm 0.5a_0$, for $\theta=60°$ and 0°, and assumed that for other angles θ the energy splitting is similar due to the cylindrical symmetry of the potential surface. The fit of the $p_{x,y}$ orbital energies was performed in a space of dimensionless normal coordinates (Q_1,ρ,ϕ) where $\rho=\sqrt{Q_2^2+Q_3^2}$, $\phi=\arctan(Q_2/Q_3)$ and (Q_1,Q_2,Q_3) are related to the displacement coordinates $(\Delta r_1,\Delta r_2,\Delta r_3)$ by [47]

$$Q_1=f\frac{1}{\sqrt{3}}(\Delta r_1+\Delta r_2+\Delta r_3), \tag{5.2a}$$

$$Q_2=f\frac{1}{\sqrt{3}}(2\Delta r_1-\Delta r_2-\Delta r_3), \tag{5.2b}$$

$$Q_3=f(\Delta r_2-\Delta r_3), \tag{5.2c}$$

where $f=2.639255a_0^{-1}$ is a constant.

The energy splitting between the $4p_x$ and $4p_y$ orbitals along the A_1 asymmetric stretch mode and our numerical fit

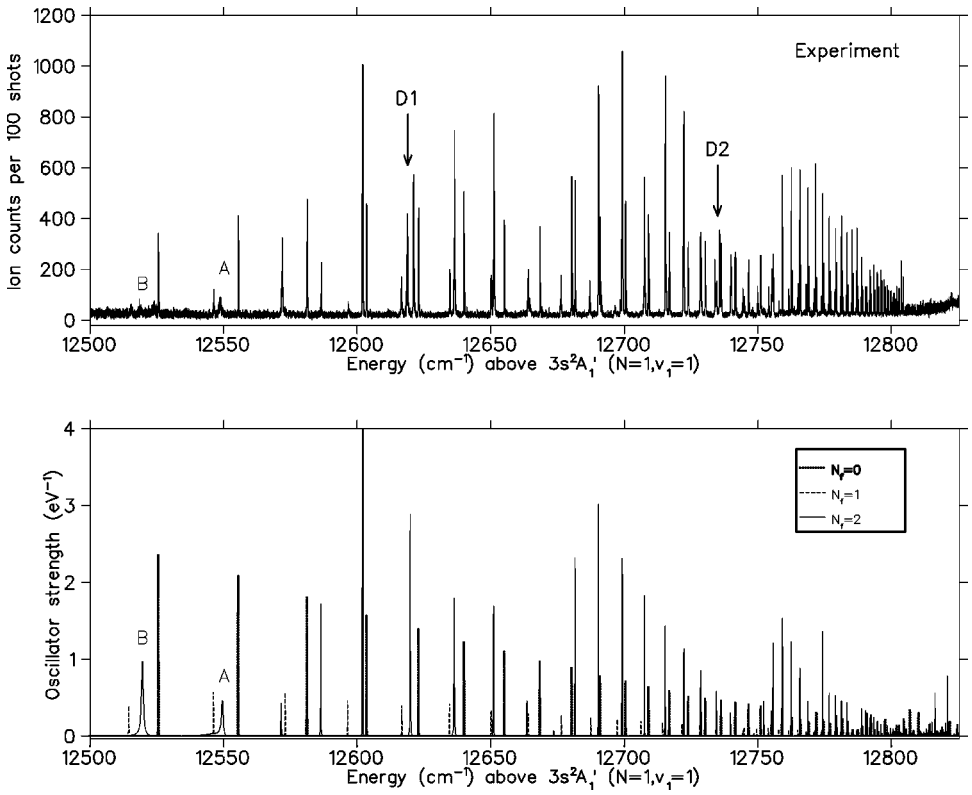

FIG. 4. Experimental photoexcitation spectrum of H_3 in the quasidiscrete region (upper panel) and calculated oscillator strength (lower panel) for $N_f=0$ (dotted line), $N_f=1$ (dashed line), and $N_f=2$ (solid line). The calculated spectrum was convoluted with a Gaussian function (the full width at half maximum is 0.2 cm^{-1}).

are shown in Fig. 2(a). With positive ρ we represent the deformation for $\phi=30°(\theta=60°)$ and with negative ρ for $\phi=90°(\theta=0°)$. Figure 2(b) shows quantum defects for several geometrical configurations in C_s arrangements. Geometries in Fig. 2(b) are labeled with the same numbers as in Table I. It can be seen that the quantum defects are nearly independent of the azimuthal coordinate ϕ.

The resulting parameters obtained from the fit are listed in Table V. In the present MQDT calculations we used the parameters obtained from the fit of $n=4$ Rydberg levels.

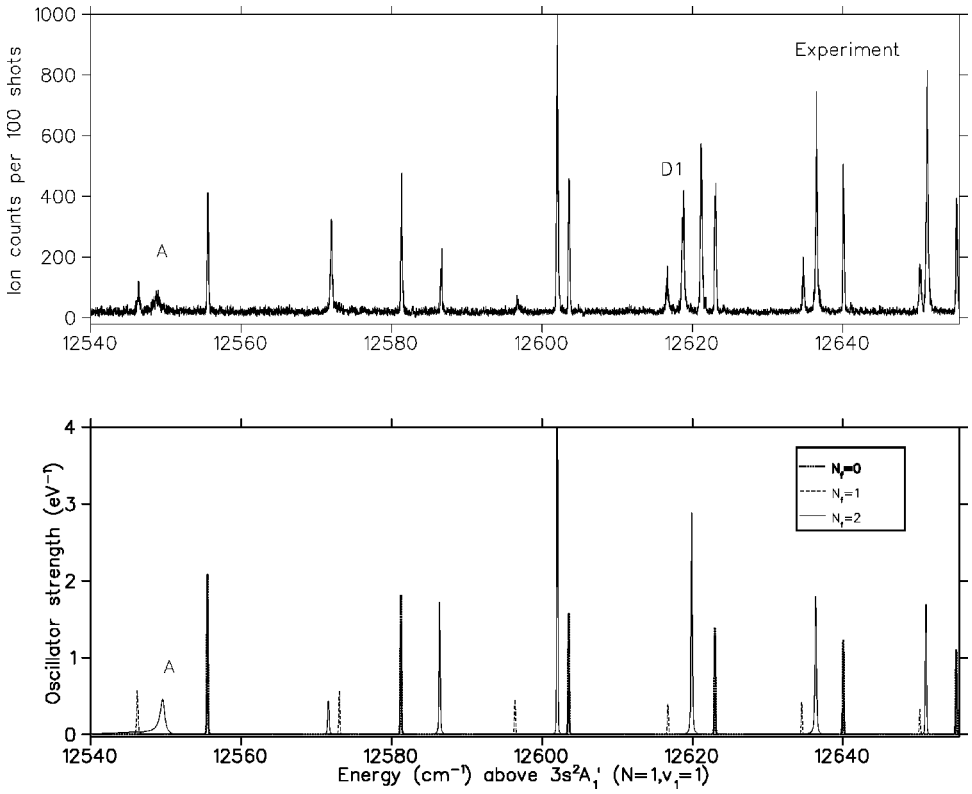

FIG. 5. Enlarged part of the experimental (upper panel) photoexcitation spectrum of H_3 in the quasidisrete region compared to the calculated (lower panel) for $N_f=0$ (dotted line), $N_f=1$ (dashed line), and $N_f=2$ (solid line).

C. Electronic transition dipole moments

The vibronic transition matrix elements needed to calculate the dipole transition amplitude in Eq. (4.8) were obtained by integration of the geometry-dependent electronic transition dipole moments $3s \rightarrow np_z, np_{x,y}$ over the initial (neutral $\{1,0^0\}$) and ionic state vibrational wave functions. Electronic transition dipole moments as functions of nuclear geometry can be obtained either from *ab initio* calculations or by the use of phase-shifted Coulomb functions $P_{\nu l}$, where ν is the effective quantum number of the Rydberg state, and l is the electronic orbital angular momentum. In Fig. 3(a) we show the energy dependence of the electronic transition dipole moments obtained from energy-normalized Coulomb functions. In this figure we also compare some *ab initio* values of the electronic transition dipole moments with those provided by the Coulomb functions for $n=3$–5. The strong energy dependence of the transition dipole moments in H_3 is induced by a Cooper minimum falling between $n=3$ and 4 [31]. The phase-shifted Coulomb functions for $3s$, $3p$, and $4p$ Rydberg states at the equilibrium geometry point are shown in Fig. 3(b). The phase shift in amplitudes between the p_z and $p_{x,y}$ radial wave functions, as well as their differing quantum defects, represent the departure from the united-atom approximation often used in MQDT treatments. Here it is important to go beyond this approximation to obtain correct Beutler-Fano autoionization profiles. The transition dipole moments obtained from the Coulomb functions were expanded in a Taylor series in stretching coordinates, with coefficients determined by a least-squares fit.

VI. EXPERIMENTAL RESULTS AND ASSIGNMENTS

A. Region below the $(N^+=1, K^+=0,\{1,0^0\})$ threshold

Figure 4 shows a comparison of the theoretical (upper panel) and experimental (lower panel) autoionization spectrum below the $(N^+=1,K^+=0,\{1,0^0\})$ ionization threshold. All levels shown here can autoionize into the $\{0,0^0\}$ vibrational continuum of H_3^+, which indeed they do. The polarization of the excitation laser beam was rotated by 30° with respect to the polarization of the ionization laser beam to excite all three series ($N_f=0$, 1, and 2) in one composite dye laser scan. Therefore the observed spectrum is a superposition of $P(N_f=0)$, $Q(N_f=1)$, and $R(N_f=2)$ branches. The three branches are shown by the dotted, dashed, and solid lines in Fig. 4. Intensities for the branches were scaled according to Eq. (4.11) for $\theta=30°$.

The photoexcitation spectrum below the $(N^+=1,K^+=0,\{1,0^0\})$ ionic limit is very similar to the two-channel MQDT spectrum discussed in Ref. [28], although here excited $N_f=2$ Rydberg states decay into four adjoining continua $(N^+=1,K^+=0,\{0,0^0\})$, $(N^+=3,K^+=0,\{0,0^0\})$, $(N^+=2,K^+=2,\{0,1^1\})$, and $(N^+=3,K^+=2,\{0,1^1\})$. Below an excitation energy of 12 550 cm^{-1}, the $N_f=2$ lines are broadened and have low intensities as can be seen in Fig. 4. Figure 5 shows a part of the quasidiscrete spectrum on an enlarged scale. The line marked as *A*, which is the $n=20$ Rydberg state converging to the $N^+=1$ ionization limit, is probably broadened by the strong interaction with the asymmetric stretch continuum above $(N^+=3,K^+=2,\{0,1^1\})$ H_3^+ ionic state, located 12 445 cm^{-1} above the $3s$ A_1' $(N'=1,K'=0,\{1,0^0\})$ H_3 state. However, an additional mechanism for line broadening and intensity loss in the observed spectrum may be due to predissociation to the repulsive ground state of H_3. The observed intensities for $N_f=2$ Rydberg states with lower ($n<20$) principal quantum number are significantly lower than those calculated (see peaks marked as *B* and *A* in Fig. 4). Two strong interloper Rydberg states appear in the quasidiscrete region, indicated as $D1$ and $D2$ in Table VI. One of them is shown in Fig. 5, indicated as $D1$. Since these two interlopers do not appear in our calculation which includes 40 ionization channels, they are likely very low-n ($n=3$ and 4) Rydberg states attached

TABLE VI. Rovibronic interlopers appearing in the H_3 photoionization spectrum.

Label [a]	$h\nu_{expt.}$ [b]	Width [c]	$h\nu_{MQDT}$ [d]	N_f	$(N^+K^+),\{v_1 v_2^{l2}\})$	n
$D1$	−212.8	0.3		2	(4,3),$\{10^0\}$	12d
$D2$	−95.8	0.3		2	(4,3),$\{10^0\}$	13d
$B1$	7.7	0.7	11.8	2	(1,0),$\{12^0\}$	5
$B2$	31.0	0.4				
$B4$	125.2	1.4	132.6	2	(1,0),$\{02^0\}$	9
$B5$	169.4	1.2	167.4	2	(2,2),$\{11^1\}$	7∼8
$B8$	234.5	0.2	234.2	0	(1,0),$\{02^0\}$	9
$B9$	317.7	0.4	256.4	2		
$B10$	318.6	0.2				
$B11$	368.4		368.3	2	(3,0),$\{12^0\}$	5
$B12$	374.3	0.3	375.5	0	(1,0),$\{22^0\}$ [e]	4
$C1$	445.6		446.0	2		
$C2$	488.4	0.5	487.3	2		
$C3$	558.0	0.5	562.3	2		
$C4$	628.7	0.4	628.7	2		
$C5$	657.2	1.1	667.1	2	(1,0),$\{20^0\}$	7
$C6$	675.0	2.8	682.5	2	(1,0),$\{20^0\}$ [f]	7
$C7$	803.5	0.4	803.5	0	(1,0),$\{20^0\}$	7
$C8$	850.5	0.5	756.6	2	(1,0),$\{03^3\}$	6
$C10$	1010.5	0.3				
$C11$	1014.7	0.2				
$C12$	1018.6	0.7	1019.5	2	(1,0),$\{30^0\}$	5
$C13$	1080.5	0.3	1084.7	2	(3,0),$\{20^0\}$	7
$C14$	1115.5					
$C15$	1212.3	0.4	1202.7	2	(1,0),$\{12^0\}$	6
$C16$	1289.4	0.3	1288.6	2	(1,0),$\{20^0\}$	8
$C17$	1340.8	0.2	1341.0	0	(1,0),$\{20^0\}$	8

[a] Resonances marked as *D*, *B*, and *C* appear in the discrete, Beutler-Fano, and continuums region, respectively.

[b] Observed energy, relative to the $(N^+=1,K^+=0,\{10^0\})$ ionic threshold, given in cm^{-1}. The experimental uncertainty is ± 0.5 cm^{-1}.

[c] Width of the observed resonance, given in cm^{-1}.

[d] Predicted energy by the MQDT calculation.

[e] An alternative assignment is $(N^+=3,K^+=0,\{12^0\})$, $n=5$.

[f] The $C6$ resonance is close to $C5$; therefore, it is also a candidate for this assignment.

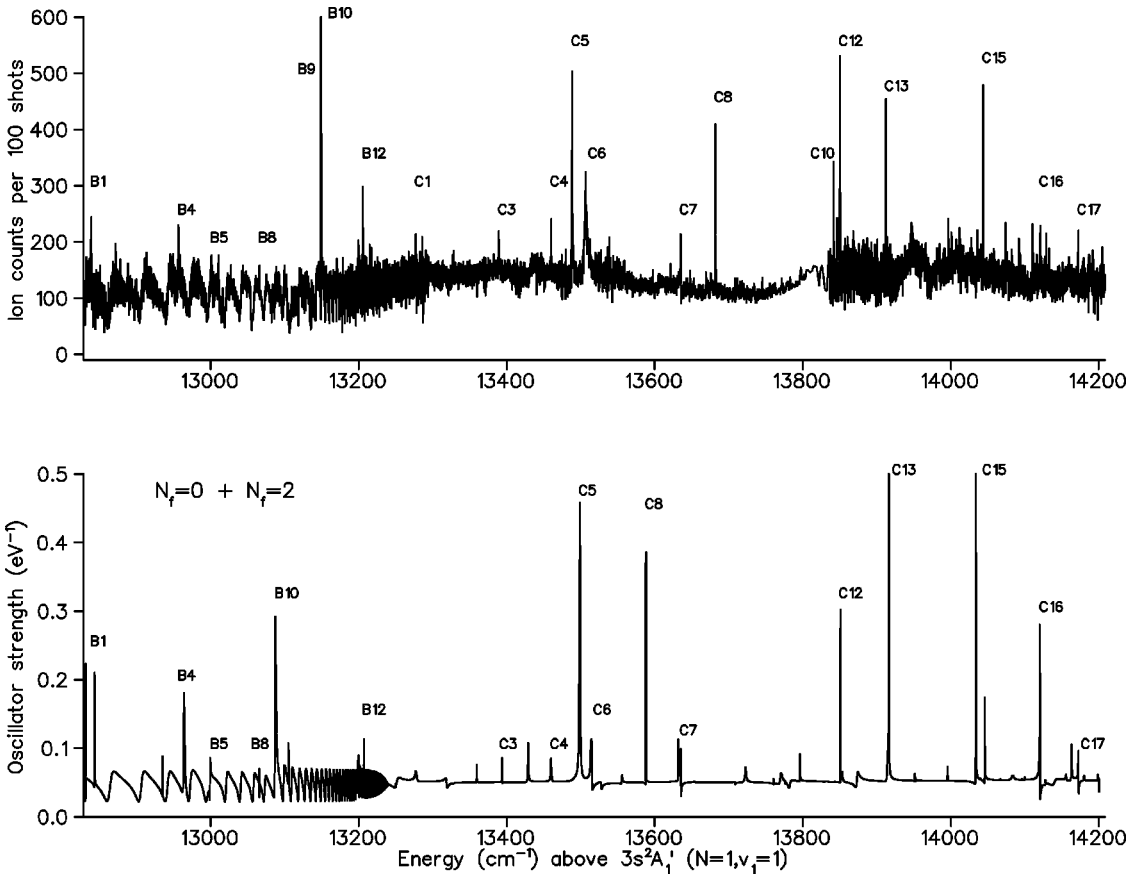

FIG. 6. Experimental photoexcitation spectrum of H_3 in the region above the $(N^+=1,K^+=0,\{1,0^0\})$ ionic limit (upper panel), and predicted oscillator strengths for $N_f=0$ and $N_f=2$ (lower panel). The resonances in the experimental spectrum are labeled *B* and *C* for the Beutler-Fano and continuum regions, respectively. Associated observed and predicted resonances are marked with the same labeling.

to highly-excited H_3^+ cores, or states with electronic angular momentum $l_f \neq 1$.

B. Spectral region above the $(N^+=1,K^+=0,\{1,0^0\})$ threshold

This spectral region was measured with parallel orientation of the excitation and ionization laser polarizations. Therefore we calculated the spectrum in this region for $\theta=0°$. Figure 6 presents the comparison of the theoretical and experimental spectrum up to the spectral region near the second-excited asymmetric stretch level of H_3^+, the $\{v_1,v_2^{l2}\}=\{0,2^0\}$ state. Due to the laser polarizations used, we expect that only $P(N_f=0)$ and $R(N_f=2)$ branch contributions should appear in the spectrum. The theoretical spectrum in Fig. 6 is a superposition of $N_f=0$ and contributions. The spectral region between the $N^+=1$ and $N^+=3$ ionic levels is referred to as the Beutler-Fano region, and it extends from 12 831 up to 13 251 cm^{-1}. The comparison of the experimental and calculated spectrum in the Beutler-Fano region is shown in Fig. 7 on an enlarged scale. The main features of this portion of the spectrum are the broad window resonances converging to the $(N^+=3,K^+=0,\{1,0^0\})$ ionic level. These broad window resonances are influenced rather slightly by the vibrational and the Jahn-Teller interactions because the rotational autoionization is much faster than autoionization induced by the vibrational coupling. The excellent agreement of these rotationally autoionizing Rydberg states with the simulation is seen in Fig. 7. To gain further understanding of the perturbations appearing in the Beutler-Fano region we excluded the $(N^+=3,K^+=0,\{1,0^0\})$ channel from the simulation shown in Fig. 7(c). Then only perturbers which are the lowest members of series converging to higher ionic limits appear. The perturbation marked as $B5$ appears as a window resonance assigned to the $7p$ member converging to the $(N^+=2,K^+=2,\{0,2^2\})$ ionic core level. The resonances $B1$ and $B4$ are also predicted by the theory and are assigned to the $5p$ $(N^+=1,K^+=0,\{1,2^0\})$ and $9p(N^+=1,K^+=0,\{0,2^0\})$ respectively. The narrow resonance labeled $B8$ is associated with the $9p$ member of $N_f=0$ branch converging to the $(N^+=1,K^+=0,\{0,2^0\})$ ionic limit. Resonance $B12$ can be associated with the $N_f=0$, $4p$ member converging to the $(N^+=1,K^+=0,\{2,2^0\})$ or with the $N_f=2$, $5p$ member converging to the $(N^+=3,K^+=0,\{1,2^0\})$ limit.

The region above the $(N^+=3,K^+=0,\{1,0^0\})$ level is referred to as the open continuum, and only the lowest members of the Rydberg series converging to H_3^+ cores with vibrational excitation higher than $\{1,0^0\}$. The smaller Franck-Condon factors for these transitions are compensated by the greater electronic transition moment. Resonances located in the open continuum region are marked with the

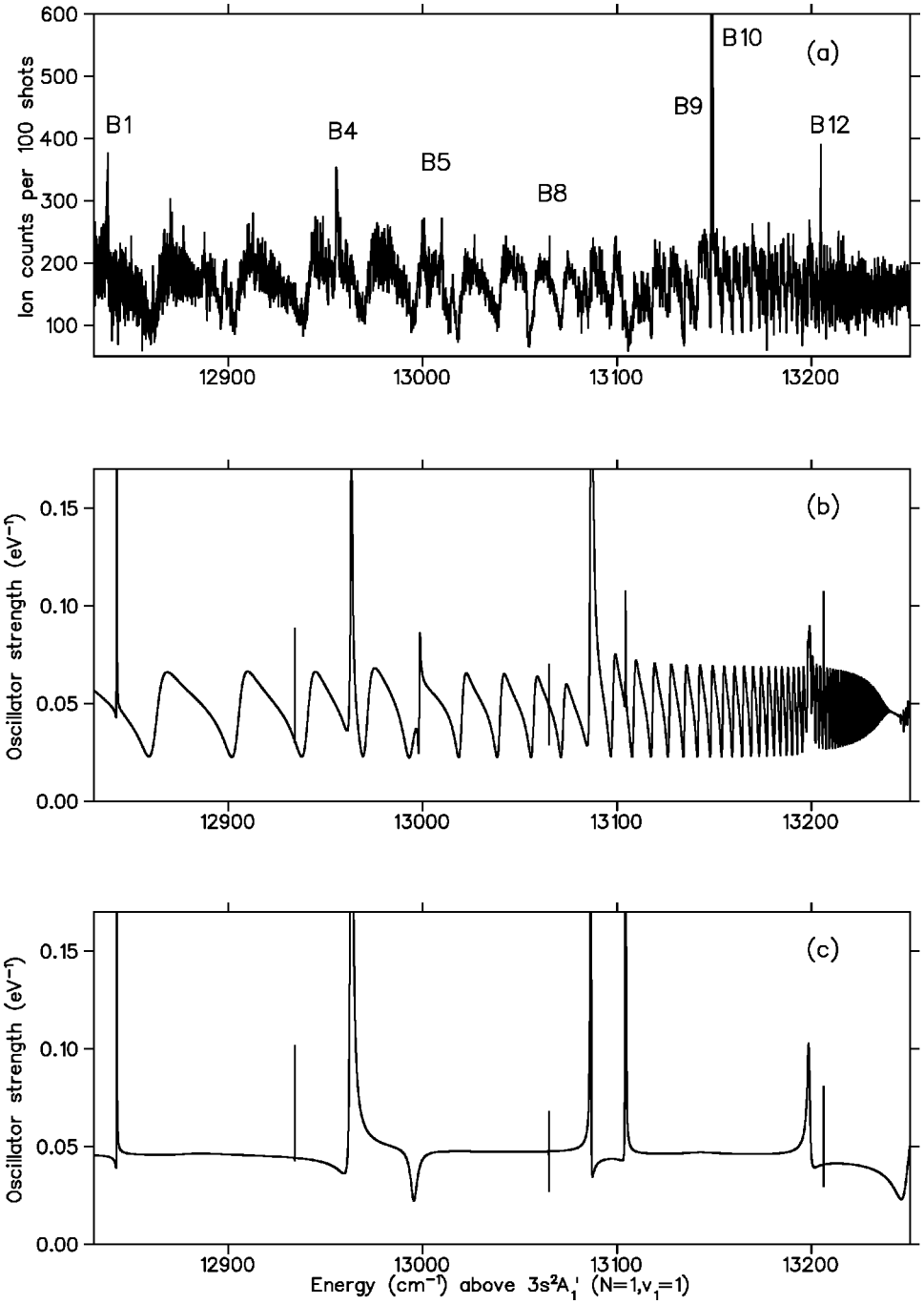

FIG. 7. Experimental photoexcitation spectrum of H_3 in the Beutler-Fano region (a) compared to the full MQDT calculation (b) and to a MQDT calculation where the threshold ($N^+=3,K^+=0,\{1,0^0\}$) was removed (c).

letter *C* in Table VI. The observed linewidth of the $N_f=0$ resonances is significantly lower than for $N_f=2$ resonances. The $N_f=0$ interloper states are coupled with the two ionization continua above the $N^+=1,K^+=0,\{0,0^0\}$ and $\{1,0^0\}$ ionic core levels. The autoionization lifetime is determined mainly by the vibrational coupling of the excited Rydberg state with the two continua, which depends on the vibrational excitation of the core to which the resonance is attached. The strength of this coupling depends on the elements of the *K* matrix obtained from the geometry dependent quantum defect surface for the A_2'' electronic state, discussed in Sec. III. In Fig. 8 we compare the line shapes of three $N_f=0$ resonances, each plotted on a scale of 10 cm^{-1}. Note that the predicted width for the resonance attached on the $\{2,0^0\}$ vibrationally excited core is significantly higher than for the $\{0,2^0\}$ core. This can be explained if we compare the first derivatives of the quantum defect function for the A_2'' (p_z) orbital along the symmetric stretch and asymmetric stretch displacement (see Fig. 1). These derivatives are a qualitative measure of the vibrational autoionization rate [49,50]. The quantum defect along the symmetric stretch coordinate is a monotonic function with nonzero first derivative at the ionic equilibrium geometry. However, the quantum defect along the asymmetric stretch coordinate *R* has a maximum at $R=0$ and zero first derivative. To first order the vibrational autoionization width for a linear harmonic oscillator should

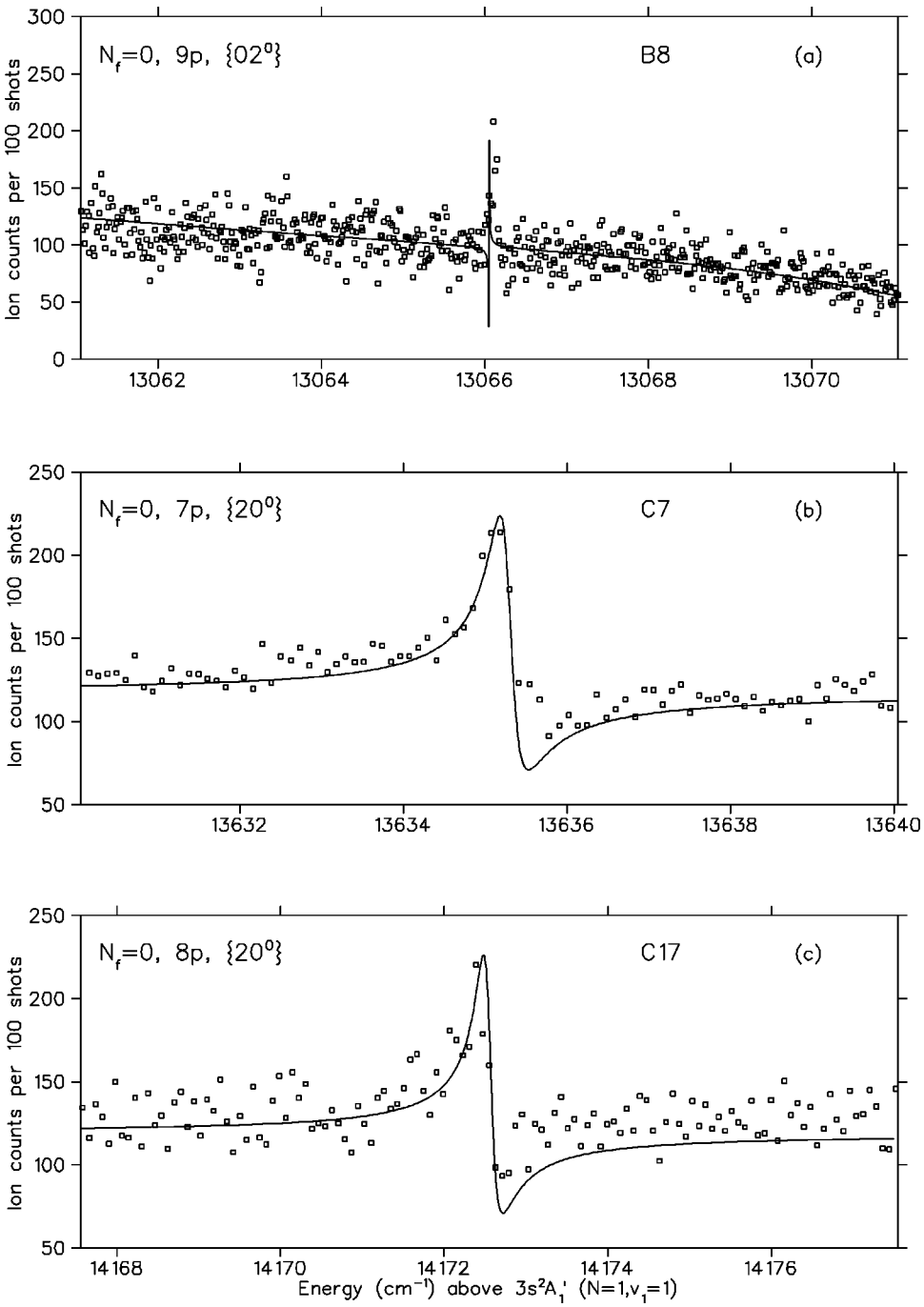

FIG. 8. Comparison of the shape of the $N_f=0$ interloper resonances appearing due to $9p$, $\{0,2^0\}$ (a), $7p$, $\{2,0^0\}$ (b), and $8p$, $\{2,0^0\}$ (c) Rydberg states. The symbols are experimental data points, and the solid line is our calculation.

then be zero. The observed (nonzero) autoionization width for the asymmetric stretch mode is due to the higher-order derivatives of the electronic potential-energy surface. The width of the predicted resonances can be estimated from a fit of the line shape with Fano's formula [51], or obtained from a time-delay analysis. For the $(n=9)$ resonance associated with the two-quanta excited asymmetric stretch mode core state [Fig. 8(a)], we predict the autoionization lifetime $\tau=1/\Gamma$ to be 40 ns. Note that this line shape is not resolved in the experiment due to the laser bandwidth. For the ($n=7$ and 8) resonances associated with the two-quanta excited symmetric stretch mode core we predict lifetimes of 290 and 500 ps, respectively, both in agreement with the experimental linewidth. The radiative- and spin-orbit-coupling-induced predissociation lifetime for the $N_f=0$ resonances is much longer (680 ns) [54] than the predicted autoionization lifetime.

Most of the assigned resonances appearing in the experimental spectrum of the open continuum are $N_f=2$ resonances. We are able to account for most of them in our MQDT calculation. Many of the observed resonances decay into the asymmetric stretch continua due to Jahn-Teller interactions represented by the nonvanishing matrix elements of the form $\langle \nu^+ A_1' | \lambda \rho \exp(-i\phi) | \nu^{+\prime} E' \rangle$, where $\nu^+\Gamma^+$ represents the excitation level and irreducible representation of the core vibration, and (ρ,ϕ) are the radial and the azi-

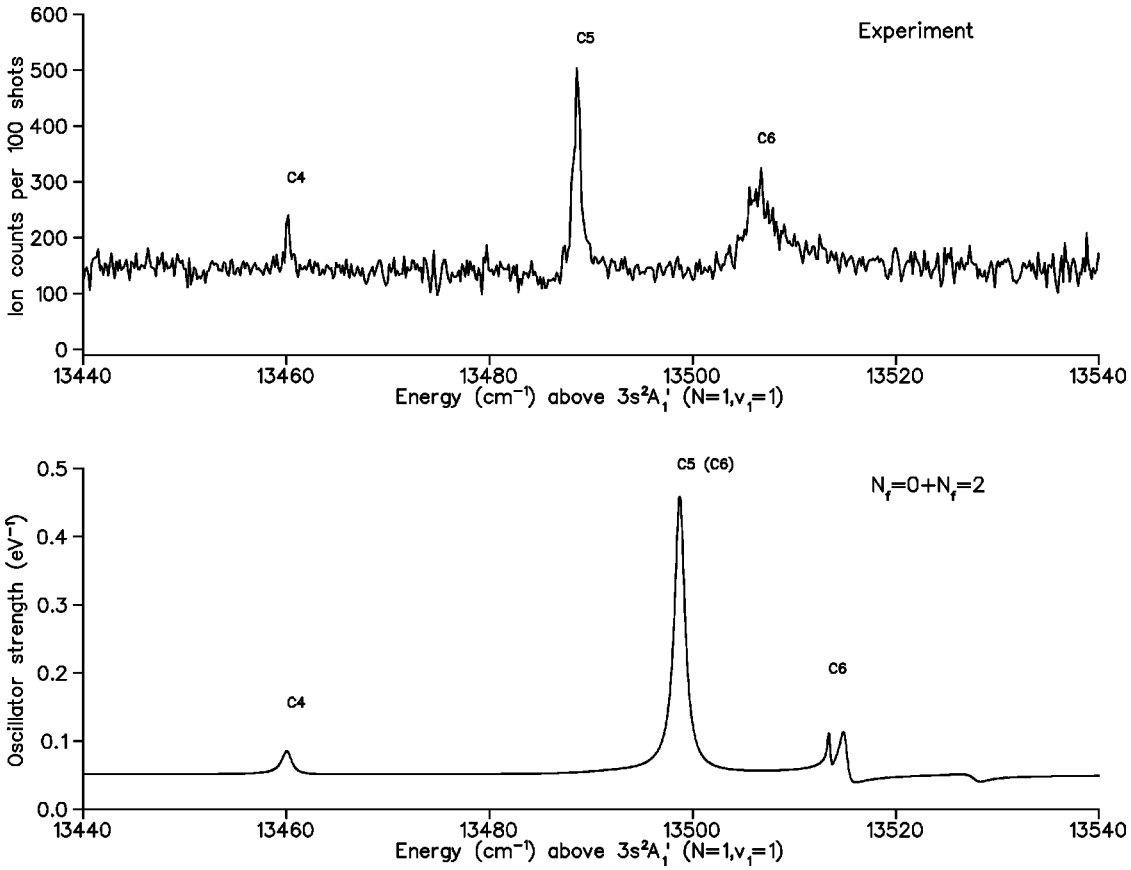

FIG. 9. Enlarged part of the experimental spectrum in the continuum region (upper panel) compared to the predicted spectrum (lower panel). The resonance marked $C6$ in the experimental spectrum is probably broadened by the strong coupling to the repulsive $2pE'$ ground state of H_3.

muthal normal coordinates. By including the Jahn-Teller interaction we allow the scattering of the Rydberg electron between $\Lambda=1$ and -1 p-electron waves in the reaction zone. Rovibronic interactions allow $N_f=2$ excited resonances to decay into the six adjoining continua $(1,0,\{0,0^0\})$, $(1,0,\{1,0^0\})$, $(3,0,\{0,0^0\})$, $(3,0,\{1,0^0\})$, $(2,2,\{0,1^1\})$, and $(3,2,\{0,1^1\})$. The calculated positions of the $N_f=2$ resonances agree to within 10 cm^{-1} with the observed peaks and windows. However the prominent resonances in the Beutler-Fano region, marked as $B9$ and $B10$ in the experiment, appear to be shifted by 50 cm^{-1} in the calculated spectrum. The analysis of the wave-function mixing coefficients indicates that this is a complex resonance appearing due to the $n=8$ interloper state converging to the second E' bending vibrationally excited core state, and that it is also strongly mixed by l uncoupling to a resonance associated with the $(N^+=3,K^+=2)$ core level. Its strength derives from borrowing intensity from several other low n-interloper states attached to highly excited H_3^+ cores. The shift of some resonances could be slightly influenced by l mixing of p and d waves. It is also possible that the potential surface for some higher vibrationally excited Rydberg states of H_3 are perturbed by the avoided crossing with one of the four core electronically excited resonance states of H_3 computed by Orel and co-workers [10].

A few of the resonances that appear in the experiment, for example $C10$ and $C11$, are not reproduced in our calculation. These are likely autoionizing d or f Rydberg states. Our calculation includes only p waves and presently does not include l mixing. The presence of nf and nd Rydberg states was previously observed in the excitation of H_3 from the vibrationless $3s$ A_1' intermediate state [29]. The symmetry of nd Rydberg states uncorrelated with the molecular frame is A_1'; therefore, the rovibrational symmetry of H_3^+ core must be A_2'' to appear in our spectra. Possible rovibrational ionic states with A_2'' symmetry are $(N^+,K^+,\Gamma^+)=(1,1,E')$, $(2,1,E')$, $(3,1,E')$, $(3,3,A_1')$, and $(4,3,A_1')$. We can tentatively assign a few of the resonances to the d Rydberg states. Resonance $D1$ can be associated with $5d$ $(N^+=3,K^+=1,\{0,3^1\})$ with an effective quantum number $\nu=4.97$, and one of the resonances $C10$ or $C11$ can be assigned to $6d$ $(N^+=3,K^+=1,\{0,3^1\})$ with an effective quantum number $\nu=5.99$. Ionic energies for $(N^+=3,K^+=1,\{0,2^2\})$ and $(N^+=3,K^+=1,\{0,3^1\})$ were calculated to be 7327.72 and 7497.53 cm^{-1}, respectively. Note that resonances $D1$ and $D2$ which appear in the discrete spectrum strongly interact with the $N_f=2$, $23p$, and $34p$ Rydberg states. It is likely that the D1 and D2 resonances belong to the nd series converging to highly rotationally excited core state $(N^+=4,K^+=3,\{1,0^0\})$ with principal quantum numbers $\nu=11.95$ and

12.96, respectively. However, higher members of this series could not clearly be confirmed.

Resonances which were reproduced by the MQDT calculation were assigned in Table VI. As an aid to the assignments we tested the sensitivity of the resonances to the removal of certain channels in the MQDT program. The missing or greatly shifted resonance was then associated with the removed channel. However, examination of the channel amplitudes shows that many resonances are strongly mixed, with substantial amplitude contributions from several channels. This makes some assignments ambiguous. A few of the resonances appear to be affected by predissociation to the repulsive ground state of H_3, as can be deduced from the linewidths and the line intensities. The example of such a resonance, marked as $C6$ in the experimental spectrum, is shown in Fig. 9 on an enlarged scale. We are attempting to study the predissociation decay paths of these broad autoionization resonances in an experiment designed to detect the neutral fragments.

VII. SUMMARY

We have interpreted the np Rydberg series of H_3 with total angular momenta $N_f=0$, 1, and 2. Using new *ab initio* quantum-defect surfaces and *ab initio* core energies of H_3^+, the present MQDT calculations, which explicitly include the 40 lowest ionization limits of H_3^+, account for most of the observed resonances and perturbations which appear in the photoexcitation and photoionization spectrum of vibrationally excited H_3. It is shown that the $N_f=0$ Rydberg series is influenced by the vibrational mixing between the ionization channels, which is determined by the nuclear-geometry-dependent $np\ A_2''$ quantum-defect surface. The dominant perturbations in the $N_f=2$ Rydberg series are due to l uncoupling and Jahn-Teller interactions between p_x and p_y orbitals in the molecular body frame. It is already clear that the present theory requires some extensions to account for all details of the spectra. Probably the most important would be to incorporate l-mixing effects and to also treat the Jahn-Teller interactions for d and f Rydberg electrons. To compare experimental results with theory for even higher rovibrational core excitations, it is necessary to include dissociative channels because higher vibrational states predissociate faster.

ACKNOWLEDGMENTS

We are indebted to Professor R. Jaquet (University of Siegen) for providing us with the rovibrational levels of H_3^+ calculated with high accuracy. This research was supported by the Deutsche Forschungsgemeinschaft (SFB 276 TP C13). The *ab initio* quantum-chemical calculations are part of Project No. 2000-050729.97 of the Schweizerischer Nationalfonds (SNF).

[1] G. Herzberg, J. Chem. Phys. **70**, 4806 (1979).
[2] I. Dabrowski and G. Herzberg, Can. J. Phys. **58**, 1238 (1980).
[3] H. Figger, W. Ketterle, and H. Walther, Z. Phys. D **13**, 129 (1989).
[4] W. Ketterle, H. Figger, and H. Walther, Z. Phys. D **13**, 139 (1989).
[5] H. Helm, Phys. Rev. Lett. **56**, 42 (1986).
[6] L. J. Lembo, H. Helm, and D. L. Huestis, J. Chem. Phys. **90**, 5299 (1989).
[7] H. Helm, in *Dissociative Recombination: Theory, Experiment and Applications*, edited by B. R. Rowe, A. Mitchell, and A. Canosa (Plenum Press, New York, 1993), pp. 145–153.
[8] M. Larsson, H. Danared, J. R. Mowat, P. Sigray, G. Sundström, L. Broström, A. Filevich, A. Källberg, S. Mannervik, K. G. Rensfelt, and S. Datz, Phys. Rev. Lett. **70**, 430 (1993).
[9] S. Datz, G. Sundström, Ch. Biedermann, L. Broström, H. Danared, S. Mannervik, J. R. Mowat, and M. Larsson, Phys. Rev. Lett. **74**, 896 (1995).
[10] A. E. Orel and K. C. Kulander, Phys. Rev. Lett. **71**, 4315 (1993); I. F. Schneider and A. E. Orel, J. Chem. Phys. **111**, 5873 (1999).
[11] I. F. Schneider, M. Larsson, A. E. Orel, and A. Suzor-Weiner, in *Dissociative Recombination: Theory, Experiments and Applications IV*, edited by M. Larsson, J. B. A. Mitchell, and I. F. Schneider (World Scientific, Singapore, 2000).
[12] S. R. Lundeen, in *Dissociative Recombination: Theory, Experiment and Applications*, edited by A. Mitchell and L. Guberman (World Scientific, Singapore, 1989), p. 182.
[13] M. J. Seaton, Rep. Prog. Phys. **46**, 167 (1983).
[14] M. Aymar, C. H. Greene, and E. Luc-Koenig, Rev. Mod. Phys. **68**, 1015 (1996).
[15] U. Fano, Phys. Rev. A **2**, 353 (1970).
[16] Ch. Jungen and O. Atabek, J. Chem. Phys. **66**, 5584 (1977).
[17] Ch. Jungen and D. Dill, J. Chem. Phys. **73**, 3338 (1980).
[18] C. H. Greene and Ch. Jungen, Adv. At. Mol. Phys. **21**, 51 (1985).
[19] S. Ross and Ch. Jungen, Phys. Rev. A **49**, 4353 (1994); **49**, 4364 (1994).
[20] Ch. Jungen, Phys. Rev. Lett. **53**, 2394 (1984).
[21] A. Giusti-Suzor and Ch. Jungen, J. Chem. Phys. **80**, 986 (1984).
[22] H. Gao, Ch. Jungen, and C. H. Greene, Phys. Rev. A **47**, 4877 (1993).
[23] J. A. Stephens and C. H. Greene, J. Chem. Phys. **103**, 5470 (1995).
[24] F. Texier and Ch. Jungen, Phys. Rev. Lett. **81**, 4329 (1998).
[25] L. Carata, A. E. Orel, and A. Suzor-Weiner, Phys. Rev. A **59**, 2804 (1999).
[26] U. Fano and K. T. Lu, Can. J. Phys. **62**, 1264 (1984).
[27] S. Pan and K. T. Lu, Phys. Rev. A **37**, 299 (1988).
[28] R. Reichle, I. Mistrík, U. Müller, and H. Helm, Phys. Rev. A **60**, 3929 (1999).
[29] M. C. Bordas, L. J. Lembo, and H. Helm, Phys. Rev. A **44**, 1817 (1991).
[30] J. A. Stephens and C. H. Greene, Phys. Rev. Lett. **72**, 1624 (1994).

[31] J. A. Stephens and C. H. Greene, J. Chem. Phys. **102**, 1579 (1995).
[32] Ch. Nager and M. Jungen, Chem. Phys. **70**, 189 (1982).
[33] W. Cencek, J. Rychlewski, R. Jaquet, and W. Kutzelnigg, J. Chem. Phys. **108**, 2831 (1998); R. Jaquet (private communication).
[34] R. Jaquet, W. Cencek, W. Kutzelnigg, and J. Rychlewski, J. Chem. Phys. **108**, 2837 (1998).
[35] R. Fink and V. Staemmler, Theor. Chim. Acta **87**, 129 (1993).
[36] T. H. Dunning, J. Chem. Phys. **90**, 1007 (1989).
[37] K. Kaufmann, W. Baumeister, and M. Jungen, J. Phys. B **22**, 2223 (1989).
[38] C. E. Dykstra and W. C. Swope, J. Chem. Phys. **70**, 1 (1979).
[39] K. Kaufmann and W. Baumeister, J. Phys. B **22**, 1 (1989).
[40] I. D. Petsalakis, G. Theodorakopoulos, and J. S. Wright, J. Chem. Phys. **89**, 6850 (1988).
[41] J. T. Hougen, J. Chem. Phys. **37**, 1433 (1962).
[42] B. M. Dinelli, S. Miller, and J. Tennyson, J. Mol. Spectrosc. **153**, 718 (1992).
[43] S. Miller and J. Tennyson, J. Mol. Spectrosc. **141**, 104 (1990).
[44] S. Miller and J. Tennyson, J. Mol. Spectrosc. **128**, 530 (1988).
[45] V. Špirko, Per Jensen, P. R. Bunker, and A. Čejchan, J. Mol. Spectrosc. **112**, 183 (1985).
[46] G. D. Carney and R. N. Porter, J. Chem. Phys. **60**, 4251 (1974).
[47] A. Staib and W. Domcke, Z. Phys. D **16**, 275 (1990).
[48] R. N. Zare, *Angular Momentum* (Wiley, New York, 1988).
[49] Ch. Jungen and S. T. Pratt, J. Chem. Phys. **106**, 9529 (1997).
[50] R. S. Berry, J. Chem. Phys. **45**, 1228 (1966).
[51] U. Fano, Phys. Rev. **124**, 1866 (1961).
[52] I. R. McNab, *Advances in Chemical Physics, '99*, edited by I. Prigogine and S. A. Rice (Wiley, New York, 1995), p. 1.
[53] T. Oka, Phys. Rev. Lett. **45**, 531 (1980).
[54] M. C. Bordas, P. C. Cosby, and H. Helm, J. Chem. Phys. **93**, 6303 (1990).